# Noise reduction of stochastic density functional theory for metals $\ensuremath{ igoldsymbol{\oslash} }$

Jake P. Vu 💿 ; Ming Chen 💌 📵

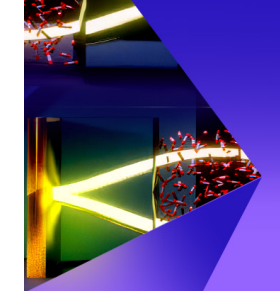


J. Chem. Phys. 160, 214125 (2024)

https://doi.org/10.1063/5.0207244







**The Journal of Chemical Physics** 

Special Topic: Polaritonics for Next Generation Materials

**Submit Today** 





# Noise reduction of stochastic density functional theory for metals

Cite as: J. Chem. Phys. 160, 214125 (2024); doi: 10.1063/5.0207244

Submitted: 6 March 2024 • Accepted: 16 May 2024 •

Published Online: 6 June 2024







Jake P. Vu<sup>a)</sup> D and Ming Chen<sup>b)</sup>



# **AFFILIATIONS**

Department of Chemistry, Purdue University, West Lafayette, Indiana 47907, USA

- a) Electronic mail: vuj@purdue.edu
- b) Author to whom correspondence should be addressed: chen4116@purdue.edu

#### **ABSTRACT**

Density Functional Theory (DFT) has become a cornerstone in the modeling of metals. However, accurately simulating metals, particularly under extreme conditions, presents two significant challenges. First, simulating complex metallic systems at low electron temperatures is difficult due to their highly delocalized density matrix. Second, modeling metallic warm-dense materials at very high electron temperatures is challenging because it requires the computation of a large number of partially occupied orbitals. This study demonstrates that both challenges can be effectively addressed using the latest advances in linear-scaling stochastic DFT methodologies. Despite the inherent introduction of noise into all computed properties by stochastic DFT, this research evaluates the efficacy of various noise reduction techniques under different thermal conditions. Our observations indicate that the effectiveness of noise reduction strategies varies significantly with the electron temperature. Furthermore, we provide evidence that the computational cost of stochastic DFT methods scales linearly with system size for metal systems, regardless of the electron temperature regime.

Published under an exclusive license by AIP Publishing. https://doi.org/10.1063/5.0207244

# I. INTRODUCTION

Metals are ubiquitous in daily life, industry, and academic research due to their unique mechanical, magnetic, and electronic properties. 1-3 Theoretical modeling of metal electronic structures is crucial for understanding their ground and excited state properties.<sup>4,5</sup> Density functional theory (DFT) is a widely used approach in materials science and condensed matter physics to accurately model the ground-state properties of metals at reasonable computational costs.<sup>4,6,7</sup> Recent studies have focused on complex metal systems, such as metal nanostructures, high-entropy alloys, and metal-support interfaces, which exhibit intriguing properties and have significant applications.<sup>8–10</sup> These materials often require large supercells in theoretical modeling, sometimes containing more than 1000 atoms. 11-13 While DFT has been effective for studying bulk metal systems, the computational cost of conventional DFT scales as  $O(N_e^3)$ , where  $N_e$  represents the number of electrons. This makes the application of conventional DFT methods to complex metal systems challenging.

Another significant challenge arises in modeling metallic systems at high electron temperatures, especially in the context of warm-dense materials relevant to fusion energy. 14 Accurate modeling of these materials requires the description of electronic structure at extremely high electron temperatures. 15 Conventional DFT methods face difficulties in modeling warm dense materials due to the requirement of a large number of partially occupied orbitals. 16 Therefore, the development of DFT methodologies that can minimize computational expenses is essential for modeling metals across various system sizes and under different conditions.

Various linear-scaling DFT methods have been developed to address the computational challenges associated with modeling These methods generally employ one of complex materials.17 two strategies: exploiting the "nearsightedness" of the electronic structure or decomposing the system into smaller, manageable subsystems. The concept of nearsightedness in electronic structure implies that the one-body density matrix,  $\rho(\mathbf{r}, \mathbf{r}')$ , decays exponentially with the distance between points  $\mathbf{r}$  and  $\mathbf{r}'$ . This property allows for the truncation of the density matrix, facilitating the use of sparse matrix techniques to achieve linear-scaling computational efficiency. 31,32 Such an approach is particularly effective for systems with large bandgap or metallic systems at high electron temperatures. 31,33 However, challenges arise when dealing with

metals at low electron temperatures due to the slow decay of  $\rho(\mathbf{r}, \mathbf{r}')$ , making the application of this principle less straightforward.<sup>3</sup> Alternatively, some methods focus on the subsystem decomposition approach, which relies on embedding theory to account for interactions between a subsystem and its environment.<sup>17</sup> This technique has shown success with non-covalently bonded systems, such as molecular clusters,<sup>24</sup> but faces significant challenges when applied to inorganic materials with covalent bonds.<sup>35</sup> Notwithstanding, certain linear-scaling DFT methods have demonstrated the ability to efficiently model metals with high electron temperatures by focusing on a localized density matrix. Nonetheless, these methods often struggle to access high-energy orbital information, which remains a limitation. 18,36,3

Stochastic DFT (sDFT) represents a significant advancement in linear-scaling DFT methodologies, uniquely addressing challenges posed by systems characterized by small or negligible fundamental gaps.<sup>38</sup> Unlike traditional DFT approaches that depend on the Kohn-Sham (KS) orbitals, sDFT calculates ground-state properties-including electron density, ground-state energy, and forces on nuclei-through the statistical averaging over a set of stochastic orbitals. Research into the application of sDFT on semiconductor materials has revealed a particularly compelling advantage: the number of stochastic orbitals required for accurate property calculation does not scale with the size of the system. This characteristic enables sDFT to achieve linear or even sublinear scaling efficiency for computations of electron density, energy per particle, and nuclear forces. The independence from explicit KS orbitals allows sDFT to effectively model systems at high electron temperatures, such as warm-dense materials (WDM), with enhanced computational efficiency.<sup>37</sup>

Inherent to sDFT, stochastic noise affects all calculated properties, presenting a significant computational challenge. To reduce this noise by an order of magnitude, the number of stochastic orbitals must be increased by two orders of magnitude, leading to a substantial rise in computational demand.<sup>42</sup> To mitigate this issue, a variety of noise reduction techniques have been developed, each leveraging different approaches to enhance computational efficiency without compromising accuracy. Among these, "overlapped embedded-fragmented sDFT" (o-efsDFT) that is based on real-space fragmentation technique, 43 "energy-window sDFT" (ew-sDFT) that is an energy-space fragmentation method, 42 and "energy window embedded-fragmented sDFT" (ew-efsDFT) that uses a hybrid strategy<sup>44</sup> have shown promise. These methods facilitate the study of semiconductors, including those with minimal bandgaps, by effectively managing stochastic noise and computational workload. Despite their success with semiconductors, the application of these noise reduction techniques to metals, particularly at varying electron temperatures, remains an area with limited exploration.4

In this study, we undertake a comprehensive benchmarking of noise reduction techniques in stochastic Density Functional Theory (sDFT), aimed at efficiently modeling metals subjected to both low and high electron temperatures. Our paper is structured to facilitate a clear understanding of these techniques and their efficacy. We begin by offering a concise introduction to sDFT, alongside a detailed overview of the various noise reduction strategies that have been developed to date. This sets the foundation for our subsequent analysis. Following the introduction, we delve into an empirical eval-

uation of these noise reduction techniques, using bulk aluminum as our test system. This evaluation encompasses simulations at both room temperature and elevated temperatures, providing insights into the performance of these methods across a range of thermal conditions. In addition, we extend our analysis to compare the computational costs associated with the ew-efsDFT method across different system sizes and temperatures. This comparison aims to elucidate the scalability and efficiency of ew-efsDFT, offering valuable perspectives on its practical application in materials science research. Through this structured approach, our study aims to illuminate the capabilities and limitations of noise reduction techniques in sDFT, contributing to the ongoing optimization of computational methodologies for the modeling of metal systems under diverse thermal conditions.

# II. STOCHASTIC DENSITY FUNCTIONAL THEORY

We initiate our discussion with a consideration of a supercell of volume V, encompassing an electron density  $\rho(\mathbf{r})$  that is discretized over a real-space grid consisting of  $N_G$  grid points. For the scenario of spin-unpolarized systems, the electron density is expressed as

$$\rho(\mathbf{r}) = 2\Sigma_i f(\varepsilon_i) \langle \mathbf{r} | \psi_i \rangle \langle \psi_i | \mathbf{r} \rangle, \tag{1}$$

where  $\psi_i(\mathbf{r}) = \langle \mathbf{r} | \psi_i \rangle$  represents the Kohn–Sham (KS) orbitals and  $\varepsilon_i$  denotes the corresponding KS orbital energies, according to the Kohn-Sham formulation of DFT. The function f(x), serving as a smearing function to accommodate the occupancy of states, is crucial for DFT calculations in metallic systems. Specifically, we employ the Fermi-Dirac distribution,

$$f(x; \mu, \beta) = \frac{1}{1 + e^{\beta(x-\mu)}},$$
 (2)

with  $\mu$  symbolizing the chemical potential and  $\beta = 1/k_BT$  representing the inverse temperature factor, where  $k_{\rm B}$  is the Boltzmann constant and T denotes the electron temperature. It is pertinent to highlight that alternative smearing functions, such as the error function, are equally viable for implementation within the scope of sDFT. The Kohn-Sham Hamiltonian,  $\hat{h}_{KS}$ , is defined as

$$\hat{h}_{KS} = \hat{t} + \hat{v}_{loc} + \hat{v}_{nl} + \hat{v}_{H} + \hat{v}_{XC}, \tag{3}$$

where  $\hat{t}$  delineates the kinetic energy term,  $\hat{v}_{loc}$  and  $\hat{v}_{nl}$  correspond to the local and nonlocal pseudopotentials, respectively,  $\hat{v}_{H}$  represents the Hartree potential, and  $\hat{v}_{XC}$  denotes the exchange-correlation potential. Consequently, the one-body reduced density matrix is succinctly described by  $\hat{\rho} = f(\hat{h}_{KS}; \mu, \beta)$ .

In sDFT, the electron density  $\rho(\mathbf{r})$  is calculated using stochastic orbitals  $|\chi\rangle$  as follows:

$$\rho(\mathbf{r}) = \langle \langle \chi | \hat{\rho} \delta(\mathbf{r} - \hat{\mathbf{r}}) | \chi \rangle \rangle_{\chi} = \langle |\xi(\mathbf{r})|^2 \rangle_{\chi}, \tag{4}$$

where  $\delta(\cdot)$  is the Dirac delta function and  $|\xi\rangle = \sqrt{\hat{\rho}}|\chi\rangle$  represents a projected stochastic orbital. The notation  $\langle \cdot \cdot \cdot \rangle_{\chi}$  denotes averaging over all samples of  $\chi$ . In practical sDFT calculations, a finite number  $(N_{\chi})$  of stochastic orbitals is employed. The stochastic orbital  $\chi(\mathbf{r})$  is constructed to satisfy  $\langle \chi(\mathbf{r})^* \chi(\mathbf{r}') \rangle_{\chi} = \delta(\mathbf{r} - \mathbf{r}')$ . Practically,  $\chi(\mathbf{r}) = \pm (\Delta V)^{-\frac{1}{2}}$ , where  $\Delta V = V/N_{\rm G}$  is the volume element of the

real-space grid, and the sign of  $\chi$  is randomly, uniformly, and independently selected for each grid point. Equation (4) becomes exact in the limit as the number of stochastic orbitals  $N_\chi \to \infty$ ; otherwise, the density obtained is a stochastic approximation.

The projection of stochastic orbitals onto the operator  $\sqrt{\hat{\rho}}$  can be efficiently approximated by expanding  $\sqrt{f(\hat{h}_{\text{KS}};\mu,\beta)}$  through polynomial series, such as Chebyshev or Newton's Interpolation polynomials. Specifically for Chebyshev polynomials, this approximation takes the form,

$$\sqrt{f(\hat{h}_{KS};\mu,\beta)} \approx \sum_{n=0}^{N_c} a_n(\mu,\beta) T_n(\hat{h}_{KS}), \tag{5}$$

where  $N_{\rm c}$  denotes the length of the polynomial chain and  $T_n(\cdot)$  are the Chebyshev polynomials. Within the framework of sDFT, the application of  $T_n(\hat{h}_{\rm KS})$  to a stochastic orbital is computed utilizing the iterative formula associated with Chebyshev polynomials, thereby facilitating a computationally efficient projection algorithm.

A property O, other than electron density, can be calculated as follows. If O is an explicit functional of electron density, it can be calculated using  $\rho$  from Eq. (4). Otherwise, O requires calculating the trace of an operator, which can be evaluated by the stochastic trace formula. In the stochastic trace formula, the trace of an operator  $\hat{O}[\rho]$  is calculated with

$$\operatorname{Tr}\left(\hat{O}[\rho]\right) = \langle \langle \chi | \hat{O}[\rho] | \chi \rangle \rangle_{\chi}, \tag{6}$$

where  $\hat{O}[\rho]$  indicates that  $\hat{O}$  depends on the electron density  $\rho$ . In a special case,  $\hat{O}[\hat{\rho}] = \hat{\rho}[\rho]\hat{A}$ , where  $\hat{A}$  is a one-body operator. In this case,

$$O = 2 \operatorname{Tr} (\hat{\rho} \hat{A}) = 2 \langle \langle \xi | \hat{A} | \xi \rangle \rangle_{\chi}. \tag{7}$$

For some other properties,  $\hat{O}$  is more complicated. For example, sDFT uses the following formula to calculate the electron density of states at energy  $\varepsilon$ :

$$D(\varepsilon) = \langle \langle \chi | \delta(\hat{h}_{KS} - \varepsilon) | \chi \rangle \rangle_{\chi} \approx \langle \langle \chi | G(\hat{h}_{KS}; \varepsilon, \sigma) | \chi \rangle \rangle_{\chi}, \tag{8}$$

where  $G(x; \varepsilon, \sigma) = \frac{1}{\sqrt{2\pi\sigma^2}} e^{-(x-\varepsilon)^2/2\sigma^2}$  is a Gaussian function. A preselected  $\sigma$  is the broadening of the Gaussian function, which determines the broadening of the density of states. The second example, electron entropy  $(S_{\rm KS})$ , is essential for finite temperature calculations involving metals. In sDFT,  $S_{\rm KS}$  can be calculated using the following formula:

$$S_{KS} = -2k_{\rm B} \langle \langle \chi | \hat{\rho} \log \hat{\rho} + (\hat{I} - \hat{\rho}) \log (\hat{I} - \hat{\rho}) | \chi \rangle \rangle_{\chi}, \tag{9}$$

where Î represents the identity operator. Both Eqs. (8) and (9) can be calculated with a Chebyshev polynomial expansion, similar to Eq. (5).

Due to the use of finite stochastic orbitals  $|\chi\rangle$ , noise exists in all quantities calculated with sDFT. This noise varies inversely with the square root of the number of stochastic orbitals,  $N_{\chi}$ , in accordance with the central limit theorem. Specifically, to reduce the stochastic fluctuation by one order of magnitude, it is necessary to

increase  $N_{\gamma}$  by two orders of magnitude. Therefore, noise reduction techniques are crucial for accurately determining properties without compromising the efficiency of sDFT. It is important to note that for many observables, such as electron density, density of states, and atomic forces, the noise does not scale with the system size. This allows sDFT to maintain linear scaling. Conversely, for properties like the energy per particle, the noise diminishes as the system size increases. This implies that fewer stochastic orbitals are required for larger systems, making sDFT a sub-linear-scaling method. However, for total energy calculations, noise amplifies with system size, challenging the linear-scaling property of sDFT. Users are encouraged to carefully assess the properties they intend to calculate with sDFT, considering the method's scalability and noise characteristics for their specific application. Our implementation of sDFT, along with all subsequent noise reduction methods discussed below, is based on the PINY\_MD package, 47 which utilizes a plane wave basis. Unlike other plane-wave-based sDFT implementations that incorporate k-point sampling,41 our approach specifically focuses on Γ-point calculations.

# A. Overlapped embedded fragmentation

The o-efsDFT method divides a supercell into fragments referred to as core regions  $(C_f)$  that are wrapped by a buffer region  $(B_f)$  to create a dressed fragment  $(D_f = C_f \cup B_f)$ , where f is the fragment index (as depicted in Fig. 1). The fragment density matrix,  $\hat{\rho}_f$ , is defined as

$$\langle \mathbf{r} | \hat{\rho}_f | \mathbf{r}' \rangle = \begin{cases} \sum_{i=1} \sqrt{f(\varepsilon_i^f; \mu_f, \beta)} \langle \mathbf{r} | \varphi_i^f \rangle \langle \varphi_i^f | \mathbf{r}' \rangle, & \mathbf{r}' \in D_f \\ 0, & \mathbf{r}' \notin D_f \end{cases}, (10)$$

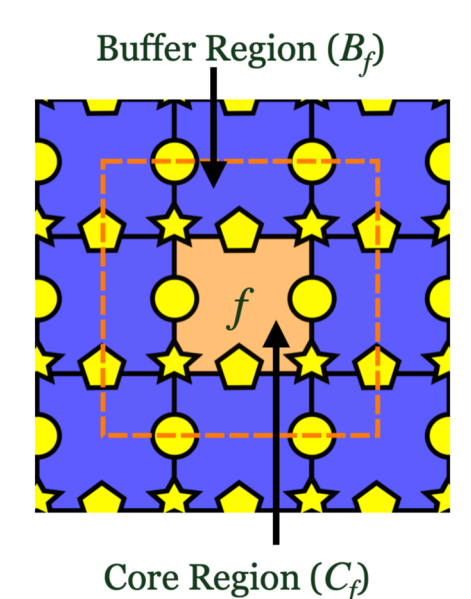


**FIG. 1.** Schematic for overlapped fragmentation.<sup>21</sup> The system is divided into overlapped fragments. Each fragment f is composed of a core region  $(C_f)$  and a buffer region  $(B_f)$  is defined around each  $C_f$ . A deterministic DFT is performed for each dressed fragment  $(D_f)$ , which is the union of  $C_f$  and  $B_f$   $(C_f \cup B_f)$ .

where  $\varphi_i^f$  are the KS orbitals for the fth fragment obtained from deterministic KS-DFT (dDFT).  $\varepsilon_i^f$  are fragment KS orbital energies.  $\mu_f$  is the chemical potential that keeps each fragment charge neutral. We want to emphasize that using o-efsDFT to model a charge-separated system needs further development. In o-efsDFT, electron density is calculated by

$$\rho(\mathbf{r}) = 2\sum_{f} \rho_{f}(\mathbf{r}) + 2\langle |\xi(\mathbf{r})|^{2} \rangle_{\chi} - 2\sum_{f} \langle |\xi_{f}(\mathbf{r})|^{2} \rangle_{\chi}, \quad (11)$$

where the fragment electron density is  $\rho_f(\mathbf{r}) = \sum_{i=1} f(\varepsilon_i^f, \mu_f, \beta)$   $\left| \varphi_i^f(\mathbf{r}) \right|^2, \xi_f(\mathbf{r}) = \sum_{i=1} \sqrt{f(\varepsilon_i^f, \mu_f, \beta)} \varphi_i^f(\mathbf{r}) \left\langle \varphi_i^f | \chi \right\rangle_{D_f}$ , and  $\left\langle \varphi_i^f | \chi \right\rangle_{D_f}$  and  $\left\langle \varphi_i^f | \chi \right\rangle_{D_f}$ , and  $\left\langle \varphi_i^f | \chi \right\rangle_{D_f}$  and  $\left\langle \varphi_i^f | \chi \right\rangle_{D_f}$  is similar with  $\hat{\rho}$ , noise in the second term of Eq. (11) will almost cancel noise in the third term. As we will demonstrate later, it is crucial to have a reasonably good fragment density matrix in order to maximize the noise reduction efficiency of sDFT.

Since the construction of  $\hat{\rho}_f$  does not require accessing stochastic orbitals, dDFT calculations are performed to converge the ground state properties of fragments before any sDFT calculations commence. As previously discussed, the similarity between  $\hat{\rho}_f$  and  $\hat{\rho}$  is critical for optimizing noise reduction efficiency. Therefore, we ensure that the same program is used in fragment dDFT calculations and the computational parameters for fragment dDFT, such as the choice of exchange-correlation functional, pseudopotentials, real space grid spacing or electron density cutoff, and wavefunction cutoff, remain consistent with those used in the sDFT calculations for the entire system. All fragment dDFT calculations exclusively utilize the  $\Gamma$ -point to ensure that the total computational costs scale linearly with system size. Although using only the  $\Gamma$ -point does not converge the k-point sampling,  $\hat{\rho}_f$  serves as a reasonably good approximation for  $\hat{\rho}$ , even for materials with small bandgaps.

Our fragmentation method significantly differs from the mixed stochastic density functional theory (MDFT) developed by White and Collins.<sup>37</sup> In MDFT, deterministic orbitals handle the dominant low-energy density matrix for the entire system explicitly, while stochastic orbitals estimate the deflated high-energy density matrix. These deterministic orbitals are updated in each self-consistent iteration within MDFT. In contrast, o-efsDFT utilizes stochastic orbitals to correct a reference system composed of fragments maintained at the same temperature. Converged dDFT calculations of fragments are performed prior to sDFT self-consistent iterations, with  $\hat{\rho}_f$  remaining fixed throughout the process.

# **B.** Energy windows

Reduction in the stochastic noise can also be achieved by dividing the occupied space into subspaces named as "energy windows." In this method, instead of projecting the stochastic orbitals onto the occupied space, the stochastic orbitals are projected onto energy windows using a set of projectors,  $\hat{\mathbf{P}}_1, \ldots, \hat{\mathbf{P}}_{N_w}$ . Here, the projector  $\hat{\mathbf{P}}_w$  is defined as

$$\hat{\mathbf{P}}_{w} = f(\hat{h}_{KS}; e_{w}, \beta) - f(\hat{h}_{KS}; e_{w-1}, \beta)$$
(12)

for  $1 \le w \le N_w$ , where  $-\infty = e_0 < e_1 < \cdots < e_{N_w} = \mu$ . In energy windows sDFT (ew-sDFT), the electron density is obtained from the sum of all the projected densities,

$$\rho(\mathbf{r}) = 2\sum_{w=1}^{N_w} \left\langle \left| \xi^{(w)}(\mathbf{r}) \right|^2 \right\rangle_{\chi} \equiv 2\sum_{w=1}^{N_w} \rho^{(w)}(\mathbf{r}), \tag{13}$$

where  $\left|\xi^{(w)}\right\rangle = \sqrt{\hat{\mathbf{P}}_w}|\chi\rangle$  is a projected stochastic orbital for window  $w\cdot\left|\xi^{(w)}\right\rangle$  are calculated simultaneously with a single polynomial expansion. We wish to highlight that the parameter  $\beta$  for the w-th window, denoted as  $\beta_w$  and ranging from  $i \leq w \leq N_w - 1$ , can differ from the physical  $\beta$ . However, in the  $N_w$ th window,  $\beta$  must align with the physical value since summing all  $\hat{\mathbf{P}}_w$  yields the Fermi–Dirac distribution function. We recommend maintaining  $\beta_w$  equal to  $\beta$  for consistency. Employing a different  $\beta_w$  typically does not enhance the overall computational efficiency of ew-sDFT, a point we will discuss further in Sec. III.

# C. Energy window embedded fragmentation

The final noise reduction method at our disposal combines the approaches used in o-efsDFT and ew-sDFT with the resulting expression for the electron density on each grid point **r**,

$$\rho(\mathbf{r}) = 2\sum_{f} \rho_{f}(\mathbf{r}) + 2\sum_{w=1}^{N_{w}} \left( \left| \zeta^{(w)}(\mathbf{r}) \right|^{2} \right)_{\chi} - 2\sum_{f} \sum_{w=1}^{N_{w}} \left( \left| \xi_{f}^{(w)}(\mathbf{r}) \right|^{2} \right)_{\chi}, \tag{14}$$

where  $\zeta^{(w)}(\mathbf{r}) = \langle \mathbf{r} | \sqrt{\hat{p}} \hat{\mathbf{P}}_w | \chi \rangle$  and  $\xi_f^{(w)}(\mathbf{r}) = \langle \mathbf{r} | \hat{p}_f \sqrt{\hat{\mathbf{P}}_w} | \chi \rangle$ . The projection operators on the energy windows are the same as ew-efsDFT, besides the last window is defined as

$$\hat{\mathbf{P}}_{N_w} = \hat{I} - \sum_{w=1}^{N_w - 1} \hat{\mathbf{P}}_w.$$
 (15)

In ew-sDFT,  $\sum_{w=1}^{N_w} \hat{\mathbf{P}}_w$  equals the density matrix  $\hat{\rho}$ , while in ew-efsDFT, it returns the identity operator,  $\hat{I}$ . In addition, the highest energy window is set to  $\varepsilon_{N_w} = \mu$  in ew-sDFT, while in ew-efsDFT, the energy windows are held fixed for the entire self-consistent procedure and are chosen to be independent of the chemical potential,  $\mu$ . This greatly simplifies the on-the-fly calculations of the chemical potential. All  $\hat{\mathbf{P}}_w$  can use non-physical  $\beta_w$  that can be different from physical  $\beta$ . Again, we recommend setting  $\beta_w$  the same as  $\beta$ . The actions of  $\sqrt{\hat{\rho}}\hat{\mathbf{P}}_w$  and  $\sqrt{\hat{\mathbf{P}}_w}$  on  $|\chi\rangle$  are obtained using a Chebyshev polynomial series.  $\rho_f$  is calculated in the same way as o-efsDFT.

# III. RESULTS

sDFT and all introduced noise reduction methods are based on the PINY\_MD package,  $^{47}$  which uses plane wave basis. Different from other plane-wave-based sDFT implementations that include k-point sampling, our approach focuses on  $\Gamma$ -point calculations. sDFT, o-efsFT, ew-sDFT, and ew-efsDFT were tested on an aluminum crystal of varying supercell sizes. Various temperatures ranging from 300 to 60 000 K were used to test metal calculations under ambient conditions as well as in warm-dense metal systems.

All calculations were performed using the Becke-Lee-Yang-Parr (BLYP) functional.  $^{48,49}$  It is important to emphasize that an exchange-correlation functional specifically tuned for warm-dense matter should be used to accurately model materials with extremely high electron temperatures. 50-52 However, this work mainly focuses on demonstrating the computational efficiency of various sDFT implementations; thus, the BLYP functional was used in all calculations. A wave function cutoff of 60.0 Ry and a density cutoff of 96.0 Ry, corresponding to a real-space grid spacing of 0.17 Å, were used for the calculations. A Troullier-Martins norm-conserving pseudopotential in Kleinman-Bylander form was employed. Throughout this study, 256 stochastic orbitals were used, regardless of the number of atoms. In the ew-sDFT and ew-efsDFT calculations, 10 energy windows are chosen by uniformly distributing between the estimated lowest KS orbital energy and estimated chemical potential. All statistical quantities were obtained using five independent runs unless explicitly stated otherwise. We used a  $2 \times 2 \times 2$  supercell containing 32 aluminum atoms as the fragment for the fragmented methods, o-efsDFT and ew-efsDFT. The core region for each fragment is  $1 \times 1 \times 1$  unit cell while the buffer region thickness is half unit cell length. The number of orbitals used in fragment dDFT calculations was selected such that the occupation numbers were truncated to less than  $1 \times 10^{-5}$ . To achieve this, we used the following number of deterministic orbitals for each system temperature: 96 orbitals (300 and 6000 K), 576 orbitals (20000 and 40 000 K), and 796 orbitals (60 000 K). For additional details about the computational parameters, please refer to the supplementary

Previous work by White and Collins has demonstrated the advantages of sDFT in studying warm dense matter.<sup>37</sup> The dDFT calculations lack information on KS orbitals with high orbital energies. Therefore, evaluating properties that require knowledge of high energy orbitals, like electron density of states, is not possible with dDFT. In Fig. 2, we demonstrate that sDFT is capable of estimating the electronic density of states even at extremely high energies. This is necessary for studying warm dense matter with high electron temperatures. Similar results were observed by White and Collins.<sup>37</sup>

Figure 3 shows the standard deviations (STD) of the electron densities calculated with various sDFT implementations at

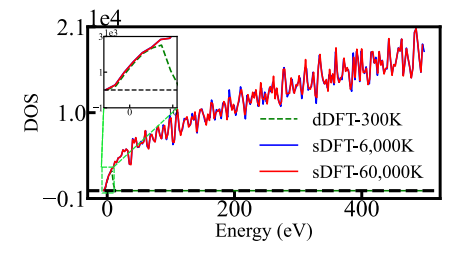


**FIG. 2.** The density of states of  $Al_{256}$  at different electron temperatures. The green dashed line is the density of states calculated from dDFT. The blue solid line and the red solid line are calculated from sDFT at temperatures 6000 and 60 000 K with Eq. (8). We used 420 deterministic orbitals to converge our dDFT calculations at 300 K while only 256 stochastic orbitals were used to converge DOS calculations in sDFT for at 6000 and 60 000 K. The inset highlights low-energy DOS.

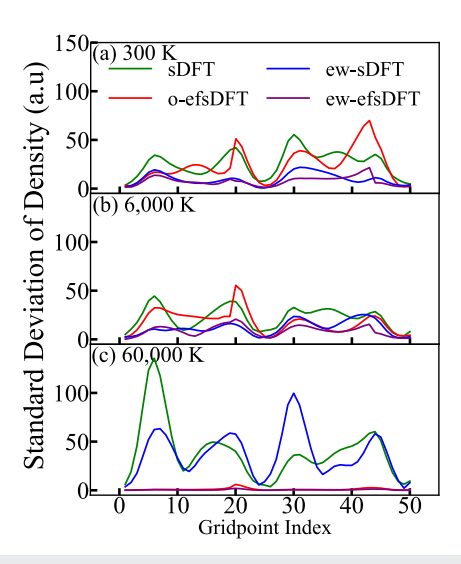


**FIG. 3.** Standard deviations (STD) of the density in sDFT and noise reduction techniques at different temperatures. We obtained the STDs over five independent trials for sDFT (green), ew-sDFT (blue), o-ef-sDFT (red), and ew-ef-sDFT (purple) at 300, 6000, and 60 000 K. We plotted the STDs for the first 50 grid points along the x axis with y=z=0.0 of Al $_{256}$ .

different electron temperatures. Panel (a) demonstrates that realspace fragmentation is not capable of reducing noise in electron density at low electron temperatures; specifically, the noise from o-efsDFT is comparable to that from sDFT, and the noise from ew-efsDFT is comparable to that from ew-sDFT. On the other hand, the energy window method works reasonably well and can reduce the noise in electron density by almost 50%. This qualitative noise reduction performance is similar when the electron temperature is increased to 6000 K, as demonstrated in panel (b) of Fig. 3. Since the Fermi-Dirac function becomes smoother at higher electron temperatures, the overlap between two neighboring energy windows becomes larger. Therefore, both ew-sDFT and ew-efsDFT become less effective at reducing noise. Real-space fragmentation still cannot efficiently reduce noise in electron density at 6000 K. When the electron temperature is increased to 60 000 K, the efficiency of noise reduction becomes very different, as shown in panel (c) of Fig. 3. First, all real-space-fragmentation-based methods, including o-efsDFT and ew-efsDFT, can significantly reduce noise in electron density. The efficiency changes for real-space fragmentation methods will be explained in the following paragraph. Second, using only ew-sDFT is not capable of reducing noise in the electron density because there is a significant overlap between two neighboring window functions.

It has been demonstrated that the noise reduction efficiency of real-space fragmentation methods depends on the difference between the fragment density matrix  $\sum_f \hat{\rho}_f$  and the system density matrix  $\hat{\rho}$ . The difference between  $\sum_f \hat{\rho}_f$  and  $\hat{\rho}$  arises for two reasons. First, a  $\Gamma$ -point calculation is performed for each fragment. The finite size error from using a small supercell in a fragment DFT calculation is one reason for the discrepancy between  $\sum_f \hat{\rho}_f$  and  $\hat{\rho}$ . Second, the fragment density matrix  $\hat{\rho}_f$  is truncated at the

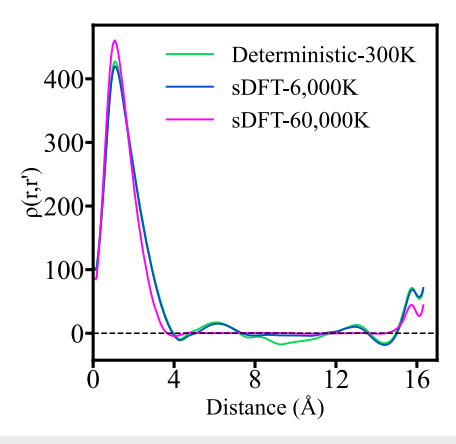


**FIG. 4.** One-dimensional slices of density matrix. The green line is the results from a 300 K deterministic DFT calculation while the blue/magenta line is from a sDFT calculation at 6000 K/60 000 K. Details of calculating the density matrix are presented in the support information.

boundary of  $D_f$ , according to Eq. (10). At 300 K,  $\hat{\rho}_f$  is very sensitive to fragment size, which can be confirmed by performing a unit cell calculation with k-point sampling. At this temperature, DFT calculations converge slowly with an increasing number of k-points (see Fig. S1 in the supplementary material). Also,  $\hat{\rho}_f$  is highly delocalized at 300 K, as shown in Fig. 4, leading to a large truncation error at the boundary of  $D_f$ . However, at 60 000 K, fragment DFT calculations converge quickly with an increasing number of k-points, and  $\hat{\rho}_f$  decays to zero much faster (see Fig. 4). Therefore, using a small supercell in a fragment DFT calculation results in  $\sum_f \hat{\rho}_f$  that is similar to  $\hat{\rho}$ . Errors associated with truncating  $\hat{\rho}_f$ 

are also negligible at 60 000 K. For hot Warm Dense Matter (WDM) at even higher temperatures, our current fragmentation implementation faces high computational demands due to the significantly larger number of orbitals required. This challenge could be mitigated by reducing the fragment size, as the density matrix becomes more localized at higher temperatures. A potential solution is to design an overlapped fragmentation of clusters, which is subject to future developments.

Noise reduction techniques can also be applied to other ground state properties, such as ground state energy and atomic forces. We list different energy terms calculated with various methods at different temperatures in Table I. We would like to emphasize that we display results only up to 20 000 K. This is due to that deterministic calculations of Al<sub>256</sub> is highly challenging at temperatures higher than 20000 K. For all ground state energies, including those for sDFT above 20 000 K, please refer to Table S1 in the supplementary material. Some energy terms, such as local pseudopotential energy, Hartree energy, and exchange-correlation energy, can be directly evaluated with electron density. The noise in these energy terms is consistent with the noise in electron density. At 300 K, the noise reduction efficiency of o-efsDFT is limited, while o-efsDFT can significantly reduce noise at 20 000 K. ew-sDFT works well at 300 K, and its noise reduction efficiency is dramatically reduced at 20 000 K. For  $E_{loc}$ ,  $E_{H}$ , and  $E_{XC}$ , ew-efsDFT performs best at all three temperatures.

Kinetic energy and non-local pseudopotential energy can be calculated using Eq. (7). Noise reduction methods for these energy terms have been developed in previous studies. <sup>42–44</sup> Real-space-fragmentation-based methods, such as o-efsDFT and ew-efsDFT, have demonstrated significant noise reduction in these energy terms. However, ew-sDFT can only achieve marginal noise reduction, even at low electron temperatures. Previous studies have indicated that,

**TABLE I.** The average energies per electron and corresponding standard deviations (STD) for various sDFT methods at different temperatures. The statistics were obtained from five independent trials for each method of sDFT used in this study. In order, the kinetic energy  $(E_K)$ , non-local pseudopotential energy  $(E_{nl})$ , local pseudopotential energy  $(E_{nl})$ , exchange–correlation energy  $(E_{NC})$ , entropy  $(TS_{NC})$ , and total energy  $(E_{tot})$  are shown in units of eV in the table. Each entry represents the average energy up to four decimal places and in parenthesis next to it, is the STD on the order of 0.1 meV.

Temperature (K)	Method	$E_{ m K}$	$E_{ m nl}$	$E_{ m loc}$	$E_{ m H}$	$E_{ m XC}$	$TS_{KS}$	$E_{ m tot}$
300	Deterministic	7.7052	-0.3639	5.4858	0.0381	-6.8521	-0.0011	-18.7095
	sDFT	7.7215(154)	-0.3666(12)	5.4858(16)	0.0494(3)	-6.8582(7)	-0.0009(0)	-18.6905(140)
	ew-sDFT	7.7059(124)	-0.3645(11)	5.4863(5)	0.0397(2)	-6.8531(2)	-0.0011(0)	-18.7084(110)
	o-efsDFT	7.7063(26)	-0.3643(3)	5.4871(13)	0.0434(2)	-6.8598(4)	-0.0010(0)	-18.7098(18)
	ew-efsDFT	7.7097(27)	-0.3643(5)	5.4861(3)	0.0385(2)	-6.8528(2)	-0.0011(0)	-18.7054(24)
6000	Deterministic	7.7702	-0.3733	5.4846	0.0395	-6.8534	-0.1193	-18.7731
	sDFT	7.8035(250)	-0.3763(14)	5.4854(12)	0.0505(2)	-6.8595(3)	-0.1198(7)	-18.7377(227)
	ew-sDFT	7.7842(205)	-0.3747(16)	5.4853(8)	0.0431(2)	-6.8556(3)	-0.1196(8)	-18.7587(191)
	o-efsDFT	7.7696(45)	-0.3735(6)	5.4852(9)	0.0424(3)	-6.8576(4)	-0.1194(10)	-18.7748(40)
	ew-efsDFT	7.7739(24)	-0.3737(3)	5.4846(3)	0.0401(1)	-6.8543(1)	-0.1199(11)	-18.7706(15)
20 000	Deterministic	8.4300	-0.4342	5.4795	0.0368	-6.8528	-1.3115	-19.3737
	sDFT	8.4596(196)	-0.4372(16)	5.4803(10)	0.0482(4)	-6.8599(4)	-1.3159(30)	-19.3464(193)
	ew-sDFT	8.4677(230)	-0.4375(17)	5.4798(10)	0.0452(6)	-6.8582(5)	-1.3161(36)	-19.3407(200)
	o-efsDFT	8.4311(22)	-0.4344(4)	5.4797(2)	0.0373(1)	-6.8538(1)	-1.3144(28)	-19.3760(32)
	ew-efsDFT	8.4300(37)	-0.4342(3)	5.4797(1)	0.0370(0)	-6.8532(1)	-1.3145(38)	-19.3766(52)

at low electron temperatures, ew-sDFT cannot reduce the noise in  ${\rm Tr}\,(\hat{\rho}\hat{O})$  only if the matrix representation of  $\hat{O}$  is diagonal-dominant in the deterministic Kohn–Sham (KS) orbital basis.<sup>42</sup> Our results suggest that the kinetic operator  $\hat{t}$  and the non-local pseudopotential operator  $\hat{v}_{\rm nl}$  tend to be diagonal-dominant in the deterministic KS orbital basis for the tested system.

Noise in the electron entropy term,  $S_{KS}$ , originates from two primary sources. The first source is the noise in electron density, which leads to noise in the Kohn-Sham Hamiltonian,  $\hat{h}_{KS}$ , and subsequently in the density matrix,  $\hat{\rho}$ . The second source is inherent in the stochastic trace formula used to calculate entropy. Despite significant reductions in electron density noise through methods, such as o-efsDFT, ew-sDFT, and ew-efsDFT, we observe that noise in TS<sub>KS</sub> persists. This observation indicates that the dominant noise contribution arises from the stochastic trace formula rather than electron density fluctuations. To delve deeper into this issue, we utilized converged electron densities,  $\rho_{\rm sDFT}$ , from sDFT or its noise-reduced variants, and performed a deterministic diagonalization of  $\hat{h}_{KS}[\rho_{sDFT}]$  to evaluate Eq. (9). This deterministic trace approach revealed a decrease in entropy noise when employing noise reduction techniques (see Table S2 in the supplementary material). This outcome underscores that the primary source of entropy noise is the stochastic trace formula, overshadowing the impact of noise reduction in electron density. Addressing the noise in the stochastic trace formula for entropy, thus, necessitates further research and development. Nevertheless, our findings indicate that the presence of significant noise in the entropy term does not adversely affect the accuracy of calculated electron densities and atomic forces.

In addition to noise-related challenges, we also identified the presence of bias or systematic errors in certain energy terms, particularly those that are non-linear functionals of electron density.<sup>55</sup>

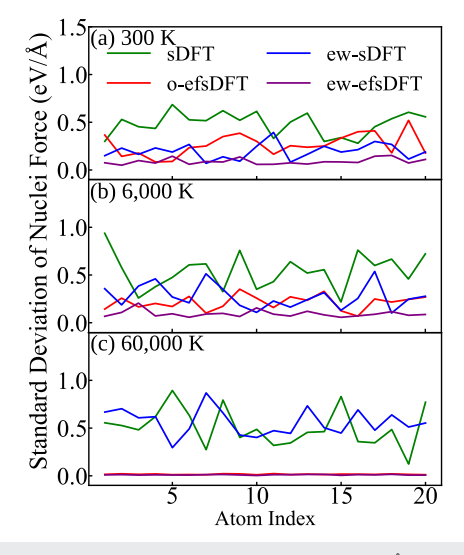


**FIG. 5.** Standard deviations (STD) of the total nuclei force (eV/Å) in sDFT and noise reduction techniques at different electron temperatures. We obtained the STD over five independent trials for sDFT (green), ew-sDFT (blue), o-ef-sDFT (red), and ew-ef-sDFT (purple) at 300, 6000, and 60 000 K. We plotted the STDs for the first 20 atoms of Al $_{256}$ .

Notably, bias is evident in  $E_{\rm H}$ ,  $E_{\rm XC}$ , and  $TS_{\rm KS}$ . Such biases are inherent to sDFT calculations, where, for instance,  $E_{\rm H}$  obtained from sDFT is significantly higher compared to dDFT calculations, despite relatively small fluctuations in  $E_{\rm H}$ . Noise reduction methods play a crucial role in mitigating these biases, largely due to their effectiveness in minimizing fluctuations in electron density. Specifically, the systematic error in all energy terms is notably reduced when employing ew-efsDFT.

Reducing noise in atomic forces is very important for determining equilibrium structures. 56,57 In Fig. 5, the STD of the force on the nuclei along the x axis  $(F_x)$  for the first 20 atoms is plotted for sDFT and noise reduction methods at electron temperatures of 300 K [panel (a)], 6000 K [panel (b)], and 60 000 K [panel (c)]. At 300 K, both o-efsDFT and ew-sDFT can marginally improve the fluctuation of nuclear forces, while ew-efsDFT performs best at 300 K. At 60 000 K, ew-sDFT is not capable of reducing noise in nuclear forces. However, both methods, o-efsDFT and ew-efsDFT, can significantly reduce the noise in nuclear forces at 60 000 K. This is consistent with the noise reduction efficiency observed in electron density at different temperatures. In Fig. 6, we highlight the efficiency of sDFT and noise reduction techniques by plotting the average STD of nuclear forces along the x-axis as a function of temperature. The efficiency of ew-sDFT is consistent with the work done by Hadad et al.4

The overlap between two neighboring window functions in ew-sDFT and ew-efsDFT can be controlled by the non-physical parameter  $\beta_w$ . Typically, the optimal choice is  $\beta_w=\beta$ . The total computational costs for both ew-sDFT and ew-efsDFT for a given system approximately equal  $N_cN_\chi$ . Here,  $N_c$  is determined by  $\max(\beta_w,\beta)$ , as the same Chebyshev polynomial expansion is used for all windowing functions. If  $\beta_w<\beta$ , the increased overlap between window functions results in decreased noise reduction efficiency. Conversely, if  $\beta_w>\beta$ ,  $N_c$  increases based on  $\beta_w$  but noise reduction efficiency is enhanced. However, the increase in computational costs due to

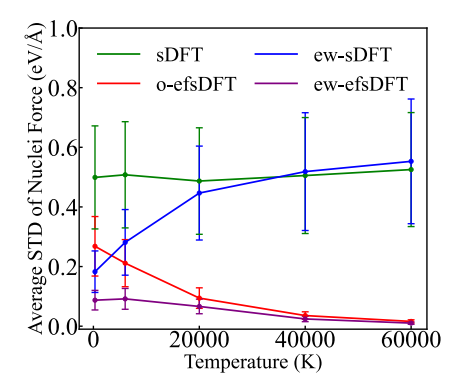


**FIG. 6.** Noise reduction efficiency in nuclei forces (eV/Å) of various sDFT methods with respect to temperature. We obtained the standard deviation (STD) of atomic force on each atom over five independent trials for each method at 300, 6000, 20 000, 40 000, and 60 000 K. We then average all STDs of different atoms and plotted the corresponding values for sDFT (green), ew-sDFT (blue), o-ef-sDFT (red), and ew-ef-sDFT (purple). The error bars indicate the fluctuations of force STD for different atoms

**TABLE II.** Comparison of different methods of obtaining statistics for nuclei forces (eV/Å). Here, we compare using sDFT and ewef-sDFT on various system sizes of Al, all of which were run at an electron temperature of 6000 K. The numbers reported in column A were a result of taking the STD across all atoms for each trial, and then taking the average of those STDs. Numbers reported in column B were a result of taking the STD for each atom across all trials, and then taking the average of those STDs. For Al $_{500}$  and Al $_{864}$ , statistics were obtained from only B.

Temperature(K)	Method	System	A	В
		Al <sub>4</sub>	0.3258	0.3332
	sDFT	$Al_{32}$	0.6225	0.5257
	SDF1	$Al_{108}$	0.5605	0.4764
6000		$Al_{256}$	0.6051	0.5078
0000		$Al_{108}$	0.1193	0.1024
	ew-efsDFT	$Al_{256}$	0.1078	0.0917
	ew-eisDr i	$Al_{500}$		0.1097
		$Al_{864}$	•••	0.1146
		$\mathrm{Al}_4$	0.3434	0.3476
	sDFT	$Al_{32}$	0.6756	0.5861
	SDF1	$Al_{108}$	0.5939	0.5079
60 000		$Al_{256}$	0.6222	0.5253
00 000	ew-efsDFT	$Al_{108}$	0.0165	0.0140
		$Al_{256}$	0.0122	0.0104
	cw-cisDr1	$Al_{500}$		0.0154
		$Al_{864}$	• • •	0.0170

a higher  $N_c$  outweighs the benefits of reducing  $N_\chi$ . Comparing ew-sDFT results at 6000 and 60 000 K, an increase in  $\beta_w$  by a factor of 10 cuts the noise in atomic force calculations by 50%, allowing  $N_\chi$  to be reduced by a factor of 4 to maintain the same noise level. Nevertheless, with  $N_c$  increasing by a factor of 10, the overall computational costs rise by a factor of 2.5.

To investigate the impact of system size on the noise reduction efficiency of sDFT and ew-efsDFT, we conducted a series of tests focusing on the atomic forces within different-sized systems. Our tests involved analyzing data from five independent trials for both sDFT and ew-efsDFT across a range of system sizes. However, due to resource constraints, we were limited to single runs for Al<sub>500</sub> and Al<sub>864</sub> when using ew-efsDFT. Given these limitations, it was crucial to design new approaches for statistical analysis of the atomic forces for these larger systems. To achieve this, we employed two distinct statistical methods for smaller system sizes, which served as a basis for comparison. The first method calculated the STD of the force on each atom across the independent trials, providing a measure of variability for individual atomic forces. The second method aggregated the forces from all atoms within a single trial and then calculated the STD, offering a holistic view of force variability within a single system snapshot. Our findings, presented in Table II, reveal no significant difference between the results obtained from these two statistical approaches. This consistency suggests that, for larger systems where conducting multiple calculations is not feasible due to resource constraints, fluctuations of nuclei forces in a single calculation can reliably represent the fluctuation of atomic forces from independent calculations. This insight is particularly valuable for efficiently assessing the noise reduction

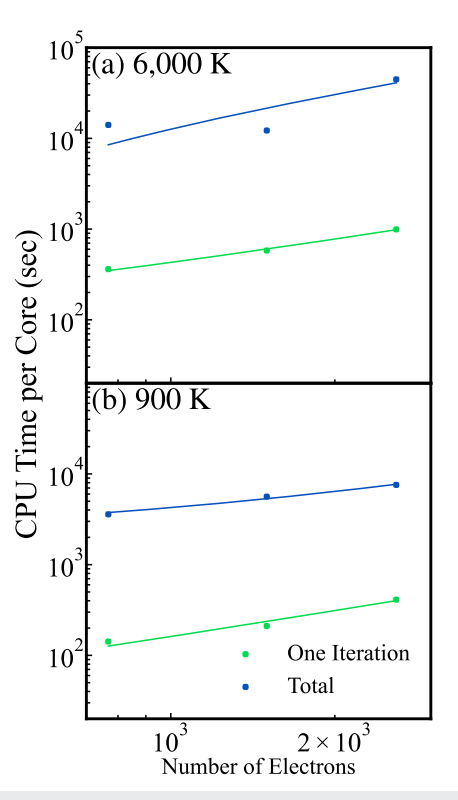


**FIG. 7.** Scaling of ew-efsDFT at 900 and 6000 K on NERSC Corri-KNL. In (a) 6000 K and (b) 900 K, the average time it took to complete one SCF iteration (blue) and the total time (green) to converge the SCF calculations were plotted against their corresponding system size.

efficiency of sDFT and ew-efsDFT in large-scale systems, indicating that even with limited data, meaningful statistical conclusions can be drawn. We want to emphasize that the equivalence of the two statistical methods may only be applicable to a crystal structure, where atoms are equivalent in such a system. We do not recommend calculating STD across different atoms in a slab model or a nanocrystal. Aside from the sDFT Al $_4$  results in Table II, which could be the result of artifacts from using a single unit cell, there appear to be no significant changes in the efficiency of noise reduction in response to system size. Since the number of stochastic orbitals is kept constant across all calculations, this suggests that the number of stochastic orbitals needed for a system is nearly independent of the system size.

Given the performance of ew-efsDFT in noise reduction for properties, such as density, ground-state energy, and force on nuclei, we tested its computational efficiency for larger systems. Our tests were conducted on the Cori-KNL and Perlmutter supercomputers at the National Energy Research Scientific Computing Center (NERSC). Calculations on Cori-KNL included Al<sub>256</sub>, Al<sub>500</sub>, and Al<sub>864</sub> at 900 and 6000 K. The same set of system sizes was tested on Perlmutter but at a system temperature of 60 000 K. The system parameters defined earlier in the discussion were applied to all six runs. In Figs. 7 and 8, we plotted the total and per iteration CPU time per core vs the number of electrons in the system on a log-log scale. Figure 7(a) presents the results for the runs at 6000 K, which shows

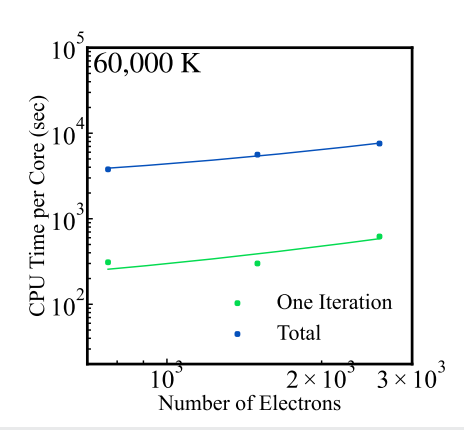


**FIG. 8.** Scaling of ew-efsDFT at 60 000 K on NERSC Perlmutter. The average time it took to complete one SCF iteration (blue) and the total time (green) to converge the SCF calculations were plotted against their corresponding system size.

that the time needed for each iteration scales as  $O(N_e^{0.83})$ , while the time needed for a single calculation scales as  $O(N_e^{0.91})$ . Figure 7(b) displays the results for the runs at 900 K, indicating that the time needed for each iteration scales as  $O(N_e^{0.86})$ , while the time needed for a single calculation scales as  $O(N_e^{0.62})$ . In Fig. 8, the run conducted on Perlmutter at 60 000 K showed that the time needed for each iteration scales as  $O(N_e^{0.63})$ , and the time needed for a single calculation scales as  $O(N_e^{0.96})$ .

The computational analysis indicates that the ew-efsDFT method scales linearly with system size. Any observed sub-linear scaling may be attributed to overheads in our calculations. Primarily, the total computational cost depends on the cumulative time required to iteratively apply the  $\hat{h}_{\rm KS}$  operator. The computational effort of applying  $\hat{h}_{\rm KS}$  once scales linearly with  $N_G$ , whether using a plane wave basis or a real-space basis with a real-space implementation of non-local pseudopotentials. The frequency of applying  $\hat{h}_{\rm KS}$  is represented by  $N_c \times N_\chi$ . Here,  $N_c$  that depends on electron temperature and the spectral range of  $\hat{h}_{\rm KS}$  remains constant regardless of system size. In addition, since the noise in many ground state properties does not increase with system size (see Table II),  $N_\chi$  is also independent of system size. Consequently, the overall computational cost exhibits a linear relationship with system size across various temperatures.

#### IV. CONCLUSIONS

In this work, we present benchmark studies on noise reduction techniques in stochastic density functional theory (sDFT) for metallic systems. Our findings indicate that the efficiency of noise reduction depends on the electron temperature. Specifically, at low electron temperatures, the energy-window-based method, ew-sDFT, outperforms the fragmentation-based approach, o-efsDFT. Conversely, at extremely high electron temperatures, o-efsDFT demonstrates superior performance over ew-efsDFT, attributed to the localized nature of the one-body density matrix. At both low and high electron temperatures, ew-efsDFT, which integrates both the energy-window and fragmentation approaches, emerges as the most efficient method. Our results further reveal that ew-efsDFT scales

linearly, enabling the efficient simulation of large metallic systems across a large range of electron temperatures. Despite ew-efsDFT's current status as the most effective noise reduction method, we observe significant residual noises in electron density, energy, and nuclear forces at low electron temperatures. This underscores the necessity for further advancements. In addition, the development of a formula to mitigate noise in electron entropy is imperative to enhance the accuracy of total energy calculations at high electron temperatures. Further studies are necessary to evaluate the application of sDFT and various noise reduction techniques to disordered or melted systems, which are typical for metals at high temperatures. We anticipate that noise reduction efficiencies observed in melted metal systems will be similar to those noted in other disordered or defected systems compared to their crystalline counterparts. 42,44 The application of overlapped fragmentation methods, which requires further development to enable the use of clusters as fragments,<sup>58</sup> represents a significant potential advancement of sDFT.

### SUPPLEMENTARY MATERIAL

Discussions on the convergence of electronic structure with system size and electron temperatures are included in the supplementary material. <sup>59,60</sup> The supplementary material also includes complete data on energies per electron with different electron temperatures, analysis of noise in entropy, details in calculating the density matrix, details of computational costs, and additional details of computational parameters.

#### **ACKNOWLEDGMENTS**

J.V. and M.C. gratefully acknowledged support from the National Science Foundation (Grant No. EAR-2246687). Resources of the National Energy Research Scientific Computing Center (NERSC), a U.S. Department of Energy Office of Science User Facility operated under Contract No. DE-AC02-05CH11231, are greatly acknowledged.

# **AUTHOR DECLARATIONS**

## **Conflict of Interest**

The authors have no conflicts to disclose.

# **Author Contributions**

Jake P. Vu: Data curation (lead); Formal analysis (lead); Investigation (supporting); Methodology (supporting); Software (supporting); Validation (lead); Visualization (lead); Writing – original draft (lead); Writing – review & editing (supporting). Ming Chen: Conceptualization (lead); Funding acquisition (lead); Investigation (lead); Methodology (lead); Project administration (lead); Resources (lead); Software (lead); Supervision (lead); Writing – review & editing (lead).

# **DATA AVAILABILITY**

The data that support the findings of this study are available from the corresponding author upon reasonable request.

#### **REFERENCES**

- <sup>1</sup> A. Bhaduri, Mechanical Properties and Working of Metals and Alloys, in Springer Series in Materials Science (Springer Nature Singapore, 2018).
- <sup>2</sup>M. E. McHenry and D. E. Laughlin, "19—Magnetic properties of metals and alloys," in *Physical Metallurgy*, 5th ed., edited by D. E. Laughlin and K. Hono (Elsevier, Oxford, 2014), pp. 1881–2008
- <sup>3</sup>H. Ehrenreich and L. Schwartz, "The electronic structure of alloy," Solid State Phys. 31, 149–286 (1976).
- <sup>4</sup>J. Aarons, M. Sarwar, D. Thompsett, and C.-K. Skylaris, "Perspective: Methods for large-scale density functional calculations on metallic systems," J. Chem. Phys. **145**, 220901 (2016).
- <sup>5</sup>C. J. Herring and M. M. Montemore, "Recent advances in real-time time-dependent density functional theory simulations of plasmonic nanostructures and plasmonic photocatalysis," ACS Nanosci. Au 3, 269–279 (2023).
   <sup>6</sup>J. W. D. Connolly and A. R. Williams, "Density-functional theory applied to
- <sup>6</sup>J. W. D. Connolly and A. R. Williams, "Density-functional theory applied to phase transformations in transition-metal alloys," Phys. Rev. B **27**, 5169–5172 (1983).
- <sup>7</sup>J. Greeley, J. K. Nørskov, and M. Mavrikakis, "Electronic structure and catalysis on metal surfaces," Annu. Rev. Phys. Chem. **53**, 319–348 (2002).
- <sup>8</sup>Z. Zhang, C. Zhang, H. Zheng, and H. Xu, "Plasmon-driven catalysis on molecules and nanomaterials," Acc. Chem. Res. **52**, 2506–2515 (2019).
- <sup>9</sup>X. Gao, R. Chen, T. Liu, H. Fang, G. Qin, Y. Su, and J. Guo, "High-entropy alloys: A review of mechanical properties and deformation mechanisms at cryogenic temperatures," J. Mater. Sci. 57, 6573–6606 (2022).
- <sup>10</sup>U. Banin, Y. Ben-Shahar, and K. Vinokurov, "Hybrid semiconductor-metal nanoparticles: From architecture to function," Chem. Mater. 26, 97–110 (2014).
- <sup>11</sup> A. H. Hakimioun, B. D. Vandegehuchte, D. Curulla-Ferre, K. Kaźmierczak, P. N. Plessow, and F. Studt, "Metal-support interactions in heterogeneous catalysis: DFT calculations on the interaction of copper nanoparticles with magnesium oxide," ACS Omega 8, 10591–10599 (2023).
- <sup>12</sup>D. Stradi, U. Martinez, A. Blom, M. Brandbyge, and K. Stokbro, "General atomistic approach for modeling metal-semiconductor interfaces using density functional theory and nonequilibrium Green's function," Phys. Rev. B 93, 155302 (2016).
- <sup>13</sup> J. Aarons, L. Jones, A. Varambhia, K. E. MacArthur, D. Ozkaya, M. Sarwar, C.-K. Skylaris, and P. D. Nellist, "Predicting the oxygen-binding properties of platinum nanoparticle ensembles by combining high-precision electron microscopy and density functional theory," Nano Lett. 17, 4003–4012 (2017).
- <sup>14</sup>M. Koenig, A. Benuzzi-Mounaix, A. Ravasio, T. Vinci, N. Ozaki, S. Lepape, D. Batani, G. Huser, T. Hall, D. Hicks *et al.*, "Progress in the study of warm dense matter," Plasma Phys. Control. Fusion 47, B441 (2005).
- <sup>15</sup>J. C. Smith, F. Sagredo, and K. Burke, "Warming up density functional theory," in *Frontiers of Quantum Chemistry*, edited by M. J. Wójcik, H. Nakatsuji, B. Kirtman and Y. Ozaki (Springer Singapore, Singapore, 2018), pp. 249–271.
- <sup>16</sup> A. Blanchet, M. Torrent, and J. Clerouin, "Requirements for very high temperature Kohn–Sham DFT simulations and how to bypass them," Phys. Plasmas 27, 122706 (2020).
- <sup>17</sup>T. Zhu, W. Pan, and W. Yang, "Structure of solid-state systems from embedded-cluster calculations: A divide-and-conquer approach," Phys. Rev. B 53, 12713–12724 (1996).
- <sup>18</sup>J. C. Prentice, J. Aarons, J. C. Womack, A. E. Allen, L. Andrinopoulos, L. Anton, R. A. Bell, A. Bhandari, G. A. Bramley, R. J. Charlton *et al.*, "The onetep linear-scaling density functional theory program," J. Chem. Phys. **152**, 174111 (2020).
- <sup>19</sup>W. Kohn, "Density functional and density matrix method scaling linearly with the number of atoms," Phys. Rev. Lett. **76**, 3168 (1996).
- <sup>20</sup>T. A. Wesolowski and Y. A. Wang, Recent Progress in Orbital-free Density Functional Theory (World Scientific, 2013).
- <sup>21</sup> E. Artacho, D. Sánchez-Portal, P. Ordejón, A. Garcia, and J. M. Soler, "Linear-scaling ab-initio calculations for large and complex systems," Phys. Status Solidi B 215, 809–817 (1999).
- <sup>22</sup>E. Hernández, M. Gillan, and C. Goringe, "Linear-scaling density-functional-theory technique: The density-matrix approach," Phys. Rev. B 53, 7147 (1996).

- <sup>23</sup>T. M. Henderson, "Embedding wave function theory in density functional theory," J. Chem. Phys. **125**, 014105 (2006).
- <sup>24</sup> P. Huang and E. A. Carter, "Advances in correlated electronic structure methods for solids, surfaces, and nanostructures," Annu. Rev. Phys. Chem. **59**, 261–290 (2008).
- <sup>25</sup>J. M. Soler, E. Artacho, J. D. Gale, A. García, J. Junquera, P. Ordejón, and D. Sánchez-Portal, "The SIESTA method for *ab initio* order-N materials simulation," J. Phys. Condens. Matter 14, 2745 (2002).
- <sup>26</sup> A. Krishtal, D. Sinha, A. Genova, and M. Pavanello, "Subsystem density-functional theory as an effective tool for modeling ground and excited states, their dynamics and many-body interactions," J. Phys. Condens. Matter 27, 183202 (2015).
- <sup>27</sup>W. Yang, "Direct calculation of electron density in density-functional theory," Phys. Rev. Lett. **66**, 1438–1441 (1991).
- <sup>28</sup>C. R. Jacob and J. Neugebauer, "Subsystem density-functional theory," WIRES Comput. Mol. Sci. 4, 325–362 (2014).
- <sup>29</sup>T. A. Wesolowski, S. Shedge, and X. Zhou, "Frozen-density embedding strategy for multilevel simulations of electronic structure," Chem. Rev. 115, 5891–5928 (2015).
- <sup>30</sup> A. Schindlmayr, "Decay properties of the one-particle Green function in real space and imaginary time," Phys. Rev. B 62, 12573–12576 (2000).
- <sup>51</sup> R. Baer and M. Head-Gordon, "Sparsity of the density matrix in Kohn-Sham density functional theory and an assessment of linear system-size scaling methods," Phys. Rev. Lett. **79**, 3962 (1997).
- <sup>32</sup>M. Challacombe, "A simplified density matrix minimization for linear scaling self-consistent field theory," J. Chem. Phys. 110, 2332–2342 (1999).
- <sup>33</sup> M. Benzi, P. Boito, and N. Razouk, "Decay properties of spectral projectors with applications to electronic structure," SIAM J. Matrix Anal. Appl. **33**, 1299–1322 (2012).
- <sup>34</sup>S. Ismail-Beigi and T. Arias, "Locality of the density matrix in metals, semiconductors, and insulators," Phys. Rev. Lett. 82, 2127 (1999).
- <sup>35</sup> J. Sun, R. C. Remsing, Y. Zhang, Z. Sun, A. Ruzsinszky, H. Peng, Z.-H. Yang, A. Paul, U. Waghmare, X. Wu, M. Klein, and J. Perdew, "Accurate first-principles structures and energies of diversely bonded systems from an efficient density functional," Nat. Chem. 8, 831–836 (2016).
- <sup>36</sup>C.-K. Skylaris, P. D. Haynes, A. A. Mostofi, and M. C. Payne, "Introducing onetep: Linear-scaling density functional simulations on parallel computers," J. Chem. Phys. 122, 084119 (2005).
- <sup>37</sup> A. J. White and L. A. Collins, "Fast and universal Kohn–Sham density functional theory algorithm for warm dense matter to hot dense plasma," Phys. Rev. Lett. 125, 055002 (2020).
- <sup>38</sup>R. Baer, D. Neuhauser, and E. Rabani, "Self-averaging stochastic Kohn–Sham density-functional theory," Phys. Rev. Lett. **111**, 106402 (2013).
- <sup>39</sup>Y. Cytter, E. Rabani, D. Neuhauser, and R. Baer, "Stochastic density functional theory at finite temperatures," Phys. Rev. B **97**, 115207 (2018).
- <sup>40</sup>R. E. Hadad, A. Roy, E. Rabani, R. Redmer, and R. Baer, "Stochastic density functional theory combined with Langevin dynamics for warm dense matter," arXiv:240111336 (2024).
- <sup>41</sup>Q. Liu and M. Chen, "Plane-wave-based stochastic-deterministic density functional theory for extended systems," Phys. Rev. B 106, 125132 (2022).
- <sup>42</sup>M. Chen, R. Baer, D. Neuhauser, and E. Rabani, "Energy window stochastic density functional theory," J. Chem. Phys. **151**, 114116 (2019).
- <sup>43</sup>M. Chen, R. Baer, D. Neuhauser, and E. Rabani, "Overlapped embedded fragment stochastic density functional theory for covalently-bonded materials," J. Chem. Phys. **150**, 034106 (2019).
- <sup>44</sup>M. Chen, R. Baer, D. Neuhauser, and E. Rabani, "Stochastic density functional theory: Real- and energy-space fragmentation for noise reduction," J. Chem. Phys. **154**, 204108 (2021).
- <sup>45</sup>R. Kosloff, "Time-dependent quantum-mechanical methods for molecular dynamics," J. Phys. Chem. **92**, 2087–2100 (1988).
- <sup>46</sup>R. Kosloff, "Propagation methods for quantum molecular dynamics," Annu. Rev. Phys. Chem. 45, 145–178 (1994).
- <sup>47</sup>M. E. Tuckerman, D. Yarne, S. O. Samuelson, A. L. Hughes, and G. J. Martyna, "Exploiting multiple levels of parallelism in molecular dynamics based

- calculations via modern techniques and software paradigms on distributed memory computers," Comput. Phys. Commun. 128, 333–376 (2000).
- <sup>48</sup> A. D. Becke, "Density-functional exchange-energy approximation with correct asymptotic behavior," Phys. Rev. A **38**, 3098–3100 (1988).
- <sup>49</sup>C. Lee, W. Yang, and R. G. Parr, "Development of the colle-salvetti correlationenergy formula into a functional of the electron density," Phys. Rev. B **37**, 785–789 (1988).
- <sup>50</sup>Z. A. Moldabekov, M. Lokamani, J. Vorberger, A. Cangi, and T. Dornheim, "Non-empirical mixing coefficient for hybrid XC functionals from analysis of the XC kernel," J. Phys. Chem. Lett. 14, 1326–1333 (2023).
- <sup>51</sup> T. Dornheim, S. Groth, and M. Bonitz, "The uniform electron gas at warm dense matter conditions," Phys. Rep. 744, 1–86 (2018).
- <sup>52</sup> M. Bonitz, T. Dornheim, Z. A. Moldabekov, S. Zhang, P. Hamann, H. Kählert, A. Filinov, K. Ramakrishna, and J. Vorberger, "Ab initio simulation of warm dense matter," Phys. Plasmas 27, 042710 (2020).
- <sup>53</sup>N. Troullier and J. L. Martins, "Efficient pseudopotentials for plane-wave calculations," Phys. Rev. B 43, 1993 (1991).
- <sup>54</sup>L. Kleinman and D. Bylander, "Efficacious form for model pseudopotentials," Phys. Rev. Lett. 48, 1425 (1982).
- <sup>55</sup>M. D. Fabian, B. Shpiro, E. Rabani, D. Neuhauser, and R. Baer, "Stochastic density functional theory," WIRES Comput. Mol. Sci. 9, e1412 (2019).
- <sup>56</sup>E. Arnon, E. Rabani, D. Neuhauser, and R. Baer, "Efficient Langevin dynamics for 'noisy' forces," J. Chem. Phys. **152**, 161103 (2020).

- <sup>57</sup> M. Chen, R. Baer, and E. Rabani, "Structure optimization with stochastic density functional theory," J. Chem. Phys. **158**, 024111 (2023).
- <sup>58</sup>E. Arnon, E. Rabani, D. Neuhauser, and R. Baer, "Equilibrium configurations of large nanostructures using the embedded saturated-fragments stochastic density functional theory," J. Chem. Phys. **146**, 224111 (2017).
- <sup>59</sup>P. Giannozzi, S. Baroni, N. Bonini, M. Calandra, R. Car, C. Cavazzoni, D. Ceresoli, G. L. Chiarotti, M. Cococcioni, I. Dabo, A. Dal Corso, S. de Gironcoli, S. Fabris, G. Fratesi, R. Gebauer, U. Gerstmann, C. Gougoussis, A. Kokalj, M. Lazzeri, L. Martin-Samos, N. Marzari, F. Mauri, R. Mazzarello, S. Paolini, A. Pasquarello, L. Paulatto, C. Sbraccia, S. Scandolo, G. Sclauzero, A. P. Seitsonen, A. Smogunov, P. Umari, and R. M. Wentzcovitch, "QUANTUM ESPRESSO: A modular and open-source software project for quantum simulations of materials," J. Phys. Condens. Matter 21, 395502 (2009).
- <sup>60</sup> P. Giannozzi, O. Andreussi, T. Brumme, O. Bunau, M. Buongiorno Nardelli, M. Calandra, R. Car, C. Cavazzoni, D. Ceresoli, M. Cococcioni, N. Colonna, I. Carnimeo, A. Dal Corso, S. de Gironcoli, P. Delugas, R. A. J. DiStasio, A. Ferretti, A. Floris, G. Fratesi, G. Fugallo, R. Gebauer, U. Gerstmann, F. Giustino, T. Gorni, J. Jia, M. Kawamura, H.-Y. Ko, A. Kokalj, E. Küçükbenli, M. Lazzeri, M. Marsili, N. Marzari, F. Mauri, N. L. Nguyen, H.-V. Nguyen, A. Otero-de-la Roza, L. Paulatto, S. Poncé, D. Rocca, R. Sabatini, B. Santra, M. Schlipf, A. P. Seitsonen, A. Smogunov, I. Timrov, T. Thonhauser, P. Umari, N. Vast, X. Wu, and S. Baroni, "Advanced capabilities for materials modelling with quantum espresso," J. Phys. Condens. Matter 29, 465901 (2017).